

Measurement of Glacier Geophysical Properties From InSAR Wrapped Phase

Richard R. Forster, Kenneth C. Jezek, *Associate Member, IEEE*, Lora Koenig, and Elias Deeb

Abstract—A method is presented for calculating longitudinal glacier strain rates directly from the wrapped phase of an interferometric synthetic aperture radar (InSAR) interferogram assuming the ice flow path is known. This technique enables strain rates to be calculated for scenes lacking any velocity control points or areas within a scene where the phase is not continuously unwrappable from a velocity control point. The contributions to the error in the estimate of the strain rate are evaluated, and recommendations for appropriate SAR and InSAR parameters are presented. An example using Radarsat-1 InSAR data of an East Antarctic ice stream demonstrates the technique for calculating longitudinal strain rate profiles and estimating tensile strength of ice (186–215 kPa) from locations of crevasse initiation. The strain rate error was found to be 17% corresponding to a tensile strength of ice error of 5.3%

Index Terms—Glaciers, interferometric synthetic aperture radar (InSAR), interferometry.

I. INTRODUCTION

PROJECTED global warming is expected to lead to continued reductions in the extent of glaciers [6]. In order to predict the spatial and temporal response, and hence potential sea level rise, models that include glacier dynamics are required. The formulation and validation of these models requires data such as glacier velocities from which, strain rates, stresses, and ice strength can be deduced. Field-based measurements of these quantities are costly to acquire due to the remote locations and harsh conditions typical of glaciers. *In situ* data that are acquired have either a limited coverage area or low spatial density [34].

A variety of remote sensing techniques have been used in the past to measure glacier velocities and calculate strain rates. Large-scale ice dynamic studies (beyond the scale of strain grids) have typically used velocity fields determined by feature tracking with repeat acquisition remote sensing data. Aerial photographs [1], [4] provide high spatial resolution (better than 1 m) but are limited by logistics and cost in areas such as Antarctica. Visible and infrared satellite images from sensors such as Landsat Thematic Mapper (TM) and SPOT are more cost effective [2], [3], [32] but are limited by clouds and long polar nights. Feature tracking using synthetic aperture radar

(SAR) [20], [36] does not have this limitation as it provides its own illumination. However, all feature-tracking techniques are limited by the presence of identifiable features and detectable displacements between acquisitions. Even with a good dataset and an automatic feature-tracking algorithm the velocity field produced is spatially irregular.

Interferometric synthetic aperture radar (InSAR) techniques can produce high spatial resolution (<30 m), high precision (<1 cm/day), uniform velocity fields over large continuous areas ($> 10\,000$ km²) for a single scene. Because the interferometric phase is only known to modulo 2π it must be integrated (unwrapped) to form a continuous phase field [8]. At this point the unwrapped phase, once corrected for topography [21], is a direct measure of the velocity gradient field. Conversion of the phase data into a velocity field requires knowledge of at least one velocity control point, either a rock outcrop representing an area of no displacement or the location of a previously measured velocity point [9]. Velocity control points for much of Antarctica are nonexistent. Even with a control point, the velocity field can only be calculated in areas where the phase is continually unwrappable from the control point. Isolated areas of low signal-to-noise ratio (SNR), shear margins and other areas of large differential velocity cause low phase coherence preventing portions of the image from being unwrapped thus, impeding glacier dynamic analysis over potentially large areas of the ice sheet using the conventional InSAR technique. In some cases control points are still desirable to improve the estimate of the baseline.

A more recent InSAR approach, “speckle tracking,” uses only the amplitude data, the coregistration offsets and ground control points to measure the ice displacement [10], [19], [25]. It has the advantage of measuring absolute displacement and succeeding in areas of low coherence, but still requires ground control points in much the same way as phase unwrapped InSAR.

In this paper we present a technique for calculating glacier geophysical properties such as longitudinal strain rates and the tensile strength of ice directly from the wrapped phase of an interferogram. Previous studies have calculated glacier strain rates from InSAR data but they are either: 1) derived from the velocity field [7], which requires additional processing steps and velocity control points or 2) derived from unwrapped phase [5] which requires phase unwrapping. InSAR data of an Antarctic glacier is used as an example to demonstrate the technique. An error analysis based on the interferometer and glacial properties is presented followed by guidelines for selection of InSAR parameters to use when estimating strain rate from wrapped phase.

Manuscript received July 20, 2001; revised April 22, 2003. This work was supported by the National Aeronautics and Space Administration under Research Grant NAG5-7871.

R. R. Forster, L. Koenig, and E. Deeb are with the Department of Geography, University of Utah, Salt Lake City, UT 84112 USA (e-mail: rick.forster.geog.utah.edu).

K. C. Jezek is with the Byrd Polar Research Center, The Ohio State University, Columbus, OH 43210 USA.

Digital Object Identifier 10.1109/TGRS.2003.815413

II. DERIVATION OF LONGITUDINAL STRAIN RATE FROM INSAR

The geometry for ice-surface velocity measurement from InSAR is shown in Fig. 1. The ice surface velocity in the flow direction (v_f) is

$$v_f = \frac{v_r}{\sin \theta \cos \beta \cos \alpha - \sin \alpha \cos \theta} \quad (1)$$

where v_r is the radar line-of-sight velocity, θ is the radar look angle, β is the angle between the radar look and ice flow direction, and α is the ice surface slope in the direction of flow [21]. Since a velocity measurement requires observations at two or more points the angles θ and β change within one measurement of v_f but for high spatial resolution data, changes are negligible between samples and the angles θ and β are assumed constant over measurement intervals < 100 m.

The velocity in the radar line-of-sight can be written

$$v_r = \frac{\phi \lambda}{4\pi T} + V_0 \sin \theta \cos \beta \quad (2)$$

where ϕ is the interferometric phase due to displacement, λ is the SAR wavelength, T is time between acquisitions and V_0 is the spatially constant component of the ice surface velocity. The first term is measured directly by the radar interferometer and based on the phase difference due to displacement between the two SAR acquisitions [21] and represents the spatial variability in velocity. This is only a relative velocity as it does not include any spatially constant velocity. The second term accounts for the spatially constant velocity (V_0) and is analogous to a baseline velocity. The \sin and \cos functions project the constant ice surface velocity to the radar line-of-sight.

The longitudinal strain rate of a glacier is the rate of change in the velocity, with respect to distance, in the direction of ice flow. Substituting (2) into (1) and differentiating yields the longitudinal strain rate shown in (3), at the bottom of the page, where ∂f is the change in distance in the direction of ice flow, $\partial \phi / \partial f$ is the phase gradient in the flow direction and $\partial \theta / \partial f = (d\theta/dy) \cos \beta$, where y is the satellite cross-track direction (Fig. 1). For spaceborne systems $\Delta \theta < 10^\circ / 100$ km and flow direction changes on large glaciers are $< 10^\circ / \text{km}$ therefore, $\partial \theta / \partial f$ and $\partial \beta / \partial f$ are negligible. The $\partial \alpha / \partial f$ term is the change in slope along the ice flow direction and results in a phase contribution due to vertical displacement. Over short spatial scales, less than an ice thickness, this vertical motion is a significant contribution to estimates of strain rate [17]. For the analysis presented here, strain rates are calculated for

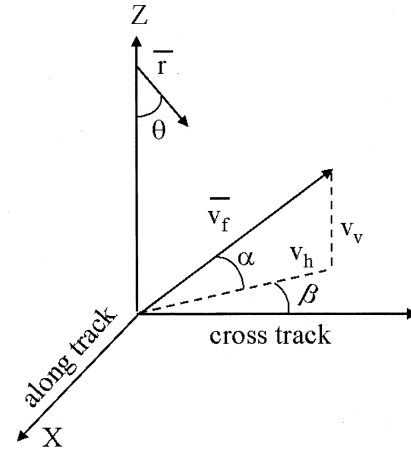


Fig. 1. Geometry for ice-surface velocity measurement from InSAR (after [21]) where \bar{r} is the radar line-of-sight, θ is the radar look angle, β is the angle between the radar look and ice flow direction, α is the ice surface slope in the direction of flow, \bar{V}_f is the velocity in the direction of flow, and V_h and V_v are the horizontal and vertical components of the ice surface velocity, respectively.

30-km-long transects with meaningful changes observed over a several kilometer scale. The ice thickness in the region is poorly constrained but estimated to be roughly 1–2 km. Therefore, the larger spatial scale strain rates of interest here are not significantly affected by the change in slope. The magnitude of the slope (α , appearing in the denominator) is insignificant for small slopes provided the angle between the radar look direction and glacier flow (β) is less than approximately 60° . The longitudinal strain rate over distances greater than an ice thickness, for instances when the above assumptions are met, reduces to

$$\dot{\epsilon}_L = \frac{\lambda}{4\pi T} \frac{\partial \phi}{\partial f} \frac{1}{\sin \theta \cos \beta} \quad (4)$$

The phase gradient in the ice flow direction ($\partial \phi / \partial f$) is the fringe rate of the interferogram in the flow direction. Therefore, the longitudinal strain rate can be calculated directly from the wrapped phase as long as the flow direction is known.

The glacier flow direction can be estimated by several techniques. Flow lines are the most direct method and have long been observed on many SAR [31] and visible and near-infrared satellite images [2]. Local slope generated from a DEM can be used with the assumption that ice flows in the direction of maximum slope [18]. The assumption of ice flow parallel to the margins can also be used to constrain the flow direction [28].

$$\begin{aligned} \dot{\epsilon}_L &= \frac{\partial V_f}{\partial f} \\ &= \frac{\frac{\partial \phi}{\partial f} \frac{\lambda}{4\pi T} - V_0 \sin \theta \sin \beta \frac{\partial \beta}{\partial f} + V_0 \cos \theta \cos \beta \frac{\partial \theta}{\partial f}}{\sin \theta \cos \beta - \alpha \cos \theta} \\ &= \frac{\left(\frac{\phi \lambda}{4\pi T} + V_0 \sin \theta \cos \beta \right) \left(\cos \theta \cos \beta \frac{\partial \theta}{\partial f} - \sin \theta \sin \beta \frac{\partial \beta}{\partial f} + \alpha \sin \theta \frac{\partial \theta}{\partial f} - \alpha \cos \theta \frac{\partial \alpha}{\partial f} \right)}{(\sin \theta \cos \beta - \alpha \cos \theta)^2} \end{aligned} \quad (3)$$

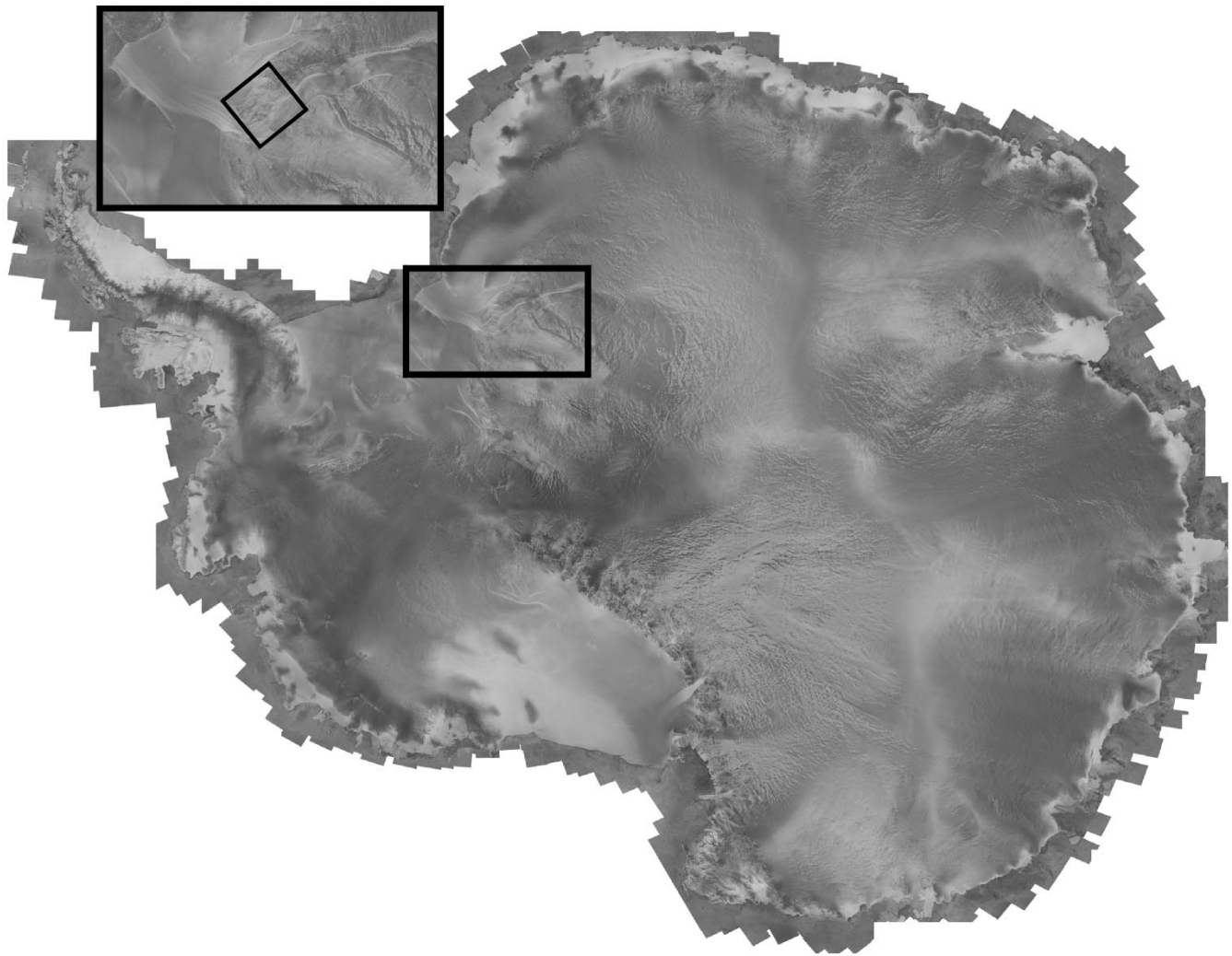


Fig. 2. Radarsat Antarctic Mapping Project (RAMP) mosaic [15] with box within inset showing image boundary of Figs. 3 and 4. The individual frame boundary is approximately 100×100 km.

III. EXAMPLE FROM ANTARCTIC INSAR DATA

A. Calculation of Strain Rate

As an example the strain rate will be calculated directly from the wrapped phase of Radarsat-1 data which has a wavelength of 5.6 cm (C-band) and operates at HH polarization. The InSAR data were acquired during the Radarsat Antarctic Mapping Project (RAMP) [15]. The entire continent of Antarctica was mapped at 25-m resolution with the Radarsat-1 during RAMP over a 30-day period in the fall of 1997 providing a static “snapshot” of the ice sheet. Since Radarsat-1 has a 24-day orbit cycle, repeat-pass InSAR data was also acquired. This example is based on analysis of an InSAR pair for the Recovery Glacier, East Antarctica.

The Recovery Glacier is a major outlet draining a portion of Queen Maud Land to the Filchner Ice Shelf (Fig. 2). Feeding the glacier is a large ice stream and tributaries, the extent of which, are easily observable from the RAMP mosaic (Fig. 2). The shear margins are well delineated by the strong returns from the intense crevassing. The InSAR scene used in the example (Fig. 3) straddles both of Recovery Glacier’s lateral shear margins. The

main trunk of this part of the ice stream is contained in the lower third of the image and ice flow is from right to left. A portion of the Shackleton Range is visible at the center right. Radarsat-1 imaged the area on September 24 and October 18, 1997 from an ascending orbit with Standard Beam mode 2 (look angle at swath center is 28°).

The single-look-complex pair was processed using three range and ten azimuth looks resulting in an interferogram with approximately 50-m pixels (Fig. 4). The topographic contribution to the phase was removed using a DEM with approximately 30-m vertical accuracy [22]. The slower moving ice on the flanks of the mountain is separated from the faster moving central core by the incoherent phase within the northern shear margin (Fig. 4).

The longitudinal strain rate along four transects was computed directly from the wrapped phase of the fringe image (Fig. 4) using (4). The transects were smoothed with a 25-pixel wide “boxcar” moving mean. The locations of the transects are shown in Figs. 3 and 4. Transect 1 [Fig. 5(a)], approximately on the centerline of Recovery Glacier, begins with undulating compressive flow for the first 18 km. At kilometer 19, the

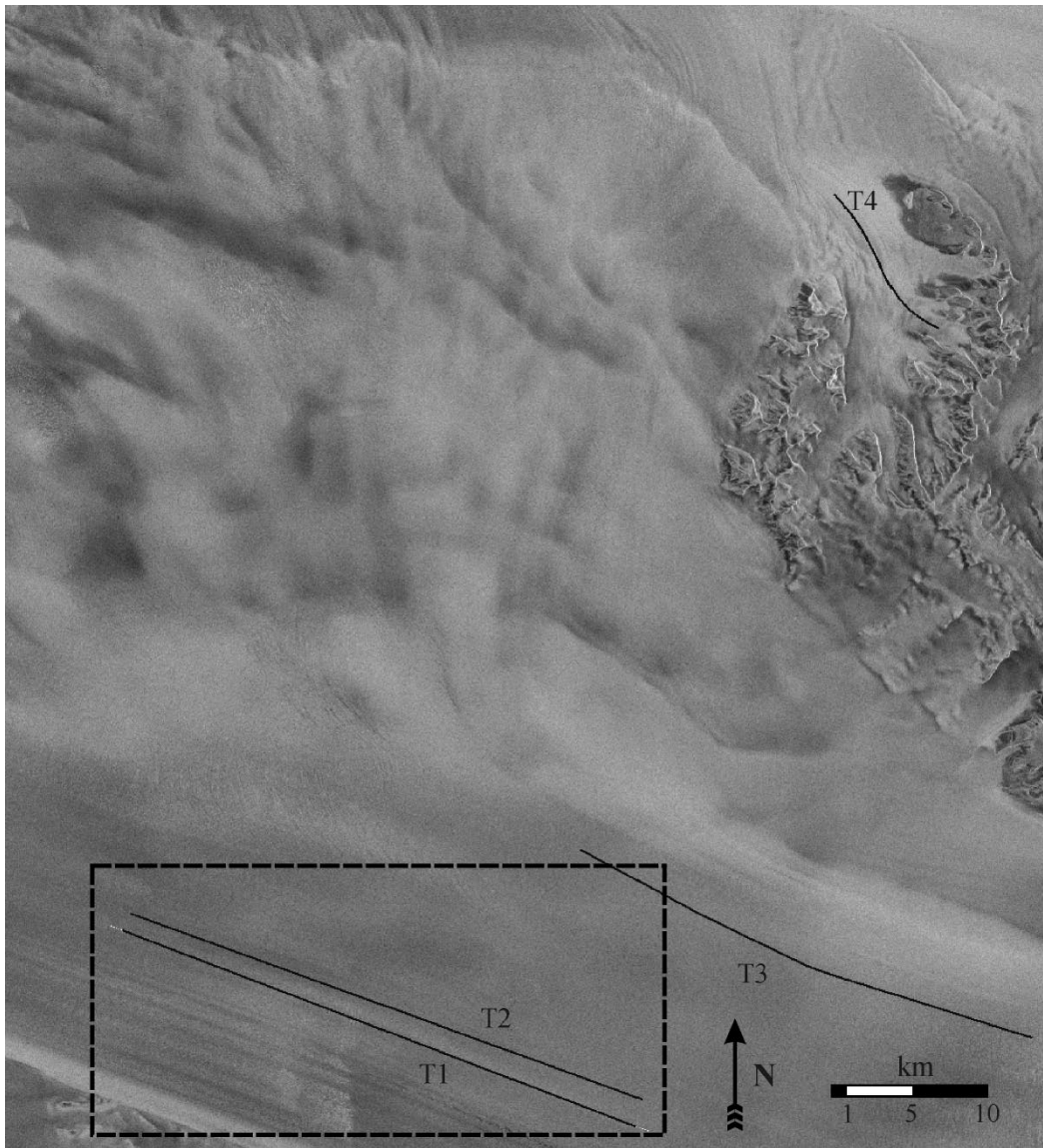


Fig. 3. Radsat-1 Recovery Glacier amplitude image with transect lines. The dashed-box is the location of Fig. 6.

strain rate changes abruptly to strong extensional flow for the next 4 km before returning with equal abruptness to compressive flow. The remainder of the transect oscillates between intermediate values of compressive and extensional flow. The oscillations in strain rate are most likely due to undulations in the basal topography. Examination of an enlarged portion of the amplitude image (Fig. 6) near the midpoint of T1 shows that it crosses an area of intense transverse crevassing. Up glacier of T1 there is no indication of transverse crevassing, thus, this represents the local crevasse initiation point.

Transect 2 parallel to T1 has similar characteristics but the undulations prior to the large increase at 19 km have a larger amplitude. The increase at 15 km to extensional flow peaks at 0.001 yr^{-1} where no crevasses are evident (Fig. 6). However, at 19 km where the strain rate peaks again, this time above 0.002 yr^{-1} , it is coincident with crevasse initiation. Transects 3 and 4 contain strain rates $<0.001 \text{ yr}^{-1}$ and show no evidence of crevassing on the amplitude image (Fig. 3). (While the strain field is more complicated toward the side of the glacier

along T3 due to some lateral shear, its effects appear to be minimal based on the parallel flow stripes in the area, Fig. 3.) The combined analysis of the transects constrains the crevasse initiation threshold to a longitudinal strain rate $>0.001 \text{ yr}^{-1}$ and $<0.0025 \text{ yr}^{-1}$ for this site where mean annual temperatures are about -30C . We assume that our computed longitudinal strain rate is approximately equal to one of the principal strain rates components. We think this is reasonably justified for transects T1, T2, and T4, which are approximately located near the midpoint of flow, and less well justified for T3, which is closer to the margin. By symmetry we expect the shear stress and strain rates to be zero near the midpoint. Van der Veen ([33, p. 141]) illustrates this fact for a West Antarctic ice stream. He shows that the shear stress fall by almost 50% of its maximum value at a distance from the outer margin equal to about 20% of the total width. Moreover for transects T1 and T2, crevasses strike approximately 70° to the transect line direction. Recognizing that the crevasses will open perpendicular to the principal extensional stress, this orientation means that only about 30% of

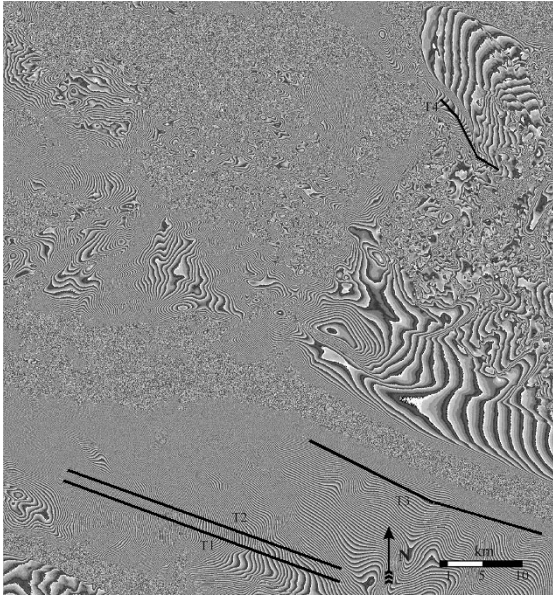


Fig. 4. Recovery Glacier fringe image with transect lines.

any residual shear strain rates contribute to the principal values [14, eq. 18, p. 39].

Previous field studies have measured the critical principal extensional strain-rate required to form transverse crevasses in temperate [12], [13], [23], [24] and polar ice [13]. The Meserve Glacier, Antarctica, with a 10 m-depth temperature of -28°C , was found to have a critical strain rate of 0.002 yr^{-1} [13]. Vornberger and Whillans [35] also adopted this value for their study of crevasses on Ice Stream B, Antarctica. The threshold of 0.002 yr^{-1} is supported by our Recovery Glacier transects (Fig. 5). A typical critical strain rate for the less brittle temperate ice is an order of magnitude higher [24].

The critical stress required to form a transverse crevasse is of more interest than the critical strain rate because it is independent of ice temperature [34] and represents the tensile strength of the ice. In Section III-B we show that the wrapped InSAR phase can be used to calculate a geophysical property of the glacier, its tensile strength.

B. Calculation of Tensile Strength

Previous work on two outlet glacier of the South Patagonian Icefield (SPI) has shown the location of crevasse initiation with SAR amplitude images combined with longitudinal strain rates calculated from InSAR velocity measurements can be used to estimate the tensile strength of ice [7]. Nunataks on the SPI provided good velocity control points allowing the unwrapped phase to be converted to an absolute velocity field. However, in the Recovery Glacier example the nunataks are isolated from the core of the ice stream by poor fringes due to large differential displacement concentrated in the shear margins. Nonetheless, the tensile strength of the ice can be estimated directly from the wrapped phase.

Assuming crevassing is controlled by the strain rate deep in the ice [34], we adopt the standard constitutive relationship to describe the ice rheology. Further we assume that lateral strain rate is small (based on the nearly parallel flow lines in

the vicinity of Transects 1 and 2) and that we are sufficiently close to the principal axes to ignore shear as expected near the glacier centerline. Then, Glen's flow law is written as

$$\dot{\epsilon}_L = A\sigma^3 \quad (5)$$

where A is the temperature dependent flow parameter and σ is the stress. Since ice fractures in response to absolute stress rather than deviatoric stress the conversion to tensile strength of ice is dependent upon the failure criteria selected. If the maximum octahedral shear-stress (von Mises) criteria [27] is used and no lateral strain is assumed then (5) predicts a tensile strength of ice to be

$$\sigma_{T_M} = \sqrt{3} \left(\frac{\dot{\epsilon}_L}{A} \right)^{1/3}. \quad (6)$$

Alternatively applying Griffith's failure criterion [14] the tensile strength of ice can be estimated as

$$\sigma_{T_G} = 2 \left(\frac{\dot{\epsilon}_L}{A} \right)^{1/3}. \quad (7)$$

The tensile strength of the ice for this section of Recovery Glacier is calculated assuming the ice fractures at a longitudinal strain rate of 0.002 yr^{-1} . This value is based on the constraints imposed by the transects (Fig. 5) coupled with crevasse locations (Figs. 3 and 6). A 10 m-depth temperature of -30°C is typical for the region [29] and used to select the flow parameter (A) value of $1.61\text{E-}09\text{ (yr}^{-1}\text{ kPa}^{-3})$ [26, p. 97]. The resulting tensile strength is 186 and 215 kPa from (7 and 8) respectively. These strengths are within the range (130–280 kPa) calculated by Vaughan [34] for several East Antarctic glaciers.

IV. ERROR ANALYSIS

The relative error in estimating longitudinal strain rate from InSAR wrapped phase is evaluated with regard to knowledge of the interferometer parameters and glacier conditions. For simplification the ice flow direction is assumed to be in the SAR range direction ($\beta = 0$). The longitudinal strain rate reduces to

$$\dot{\epsilon}_L = \frac{\lambda}{4\pi T} \frac{\partial\phi}{\partial f} \frac{1}{\sin\theta}. \quad (8)$$

For notation clarification, let $s = \partial\phi/\partial f$, then the error in the longitudinal strain rate is

$$d\dot{\epsilon}_L = \frac{\partial\dot{\epsilon}_L}{\partial s} ds = \frac{\lambda}{4\pi T} \frac{1}{\sin\theta} ds \quad (9)$$

where $ds = d(\partial\phi/\partial f)$ is the error in the phase gradient in the flow direction as measured by the interferometer.

The phase measured at the interferometer (ϕ_M) is the result of two separate physical mechanisms. There is a contribution from the topography (ϕ_Z) and from the displacement of the ice (ϕ_D) occurring between the two observation times. The phase due to displacement (ϕ_D) including the error terms ($\delta\phi$) is

$$\phi_D + \delta\phi_D = \phi_M + \delta\phi_M - (\phi_Z + \delta\phi_Z). \quad (10)$$

The error in the measured phase is the phase noise of the interferometer ($\delta\phi_{\text{Noise}}$), therefore, the error in the phase due to displacement can be written as

$$\delta\phi_D = \delta\phi_{\text{Noise}} - \delta\phi_Z. \quad (11)$$

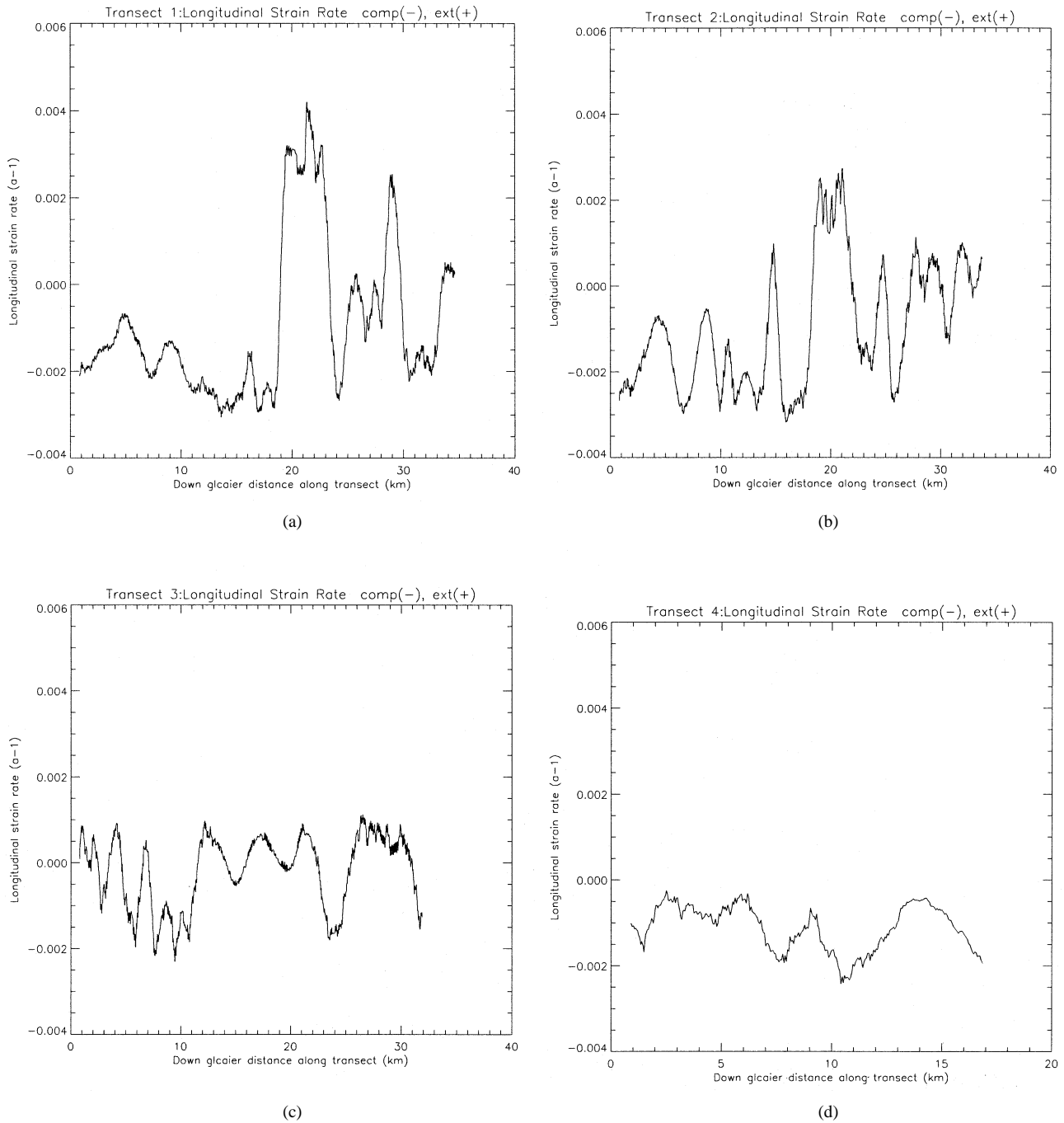


Fig. 5. Longitudinal strain rate for transects (a) T1, (b) T2, (c) T3, and (d) T4 with locations shown in Figs. 3 and 4.

The phase noise can be determined by the coherence (ρ) and the number of looks (N) used to generate the interferogram [30]

$$\delta\phi_{\text{Noise}} = \frac{\sqrt{1-\rho}}{\sqrt{N}\rho}. \quad (12)$$

The phase due to topography is

$$\phi_Z \approx \frac{-4\pi B \cos(\theta - \xi)z}{\lambda \sin \theta r_0} \quad (13)$$

where B is the magnitude of the interferometric baseline, ξ is the tilt angle of the baseline from the horizontal, z is the elevation

and r_0 is the slant range distance from the SAR [11], [16]. The accumulative error in the displacement phase is then

$$\delta\phi_D = \frac{4\pi}{\lambda \sin \theta r_0} [z \cos(\theta - \xi)dB + B \cos(\theta - \xi)dz + Bz \sin(\theta - \xi)d\xi] + \frac{\sqrt{1-\rho}}{\sqrt{N}\rho}. \quad (14)$$

The baseline can also be described by the components perpendicular (B_n) and parallel (B_p) to the look direction

$$B_n = B \cos(\theta - \xi) \quad B_p = B \sin(\theta - \xi). \quad (15)$$

The corresponding error in the phase gradient (ds) is shown in (16), at the bottom of the next page, where Δf is the distance

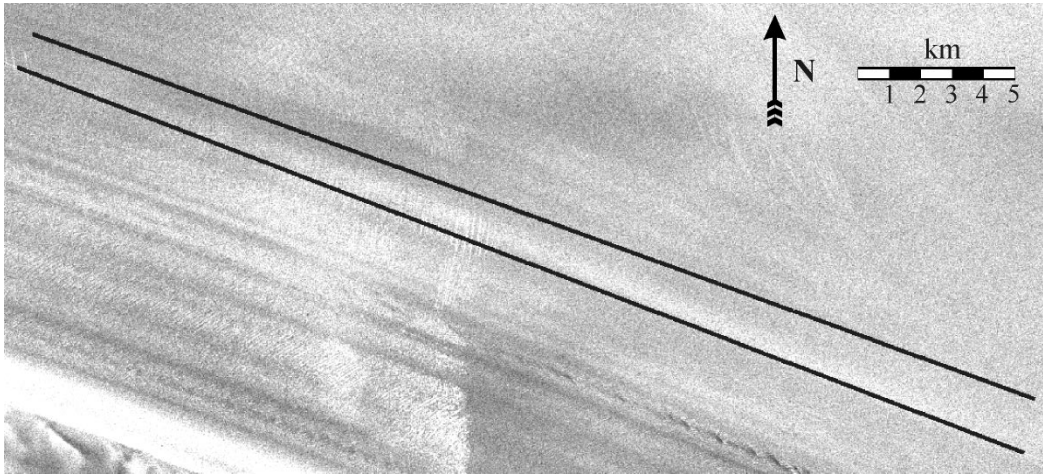


Fig. 6. Enlarged portion of Fig. 3 showing crevassed area.

TABLE I
VARIABLES CONTRIBUTING TO THE ERROR IN LONGITUDINAL STRAIN RATE [(16) AND (17)]. EXAMPLE VALUES ARE FROM THE RECOVERY GLACIER SCENE (FIG. 4). THE PERCENT ERROR IS EVALUATED OVER A TYPICAL RANGE OF THE VARIABLES

Variable	Description	Example value	Range for E_r	Error (%)
λ	Wavelength	5.6 cm	5.6 – 24 cm	see Fig. 7
θ	Look angle	28°	20 – 60°	see Fig. 7
B_n	Baseline	200 m	50 – 500 m	4.5 – 42
dB_n	Relative baseline error	10 cm	1 – 100 cm	17 – 17
ξ	Baseline tilt angle	20°	0 – 90°	15 – 8.0
$d\xi$	Tilt angle error	0.03°	1.0 – 0.001°	17 – 17
ρ	Coherence	0.7	0.3 – 0.9	17 – 17
N	Number of looks	13	1 – 20	17 – 17
dz	Relative elevation error	30 m	1 – 50 m	1.4 – 28
z	Elevation	500 m	0 – 4 km	17 – 17
s	Phase gradient	3 cyc./km	1 – 10 cyc./km	50 – 5.0

in the flow direction between the successive phase measurement locations. The relative error in strain rate is then

$$E_R = \frac{d\dot{\epsilon}_L}{\dot{\epsilon}_L} = \frac{ds}{s}. \quad (17)$$

Using typical values for the Recovery Glacier example in (16), shown in Table I, and evaluating (17) yields a longitudinal strain rate error of 17%. The error in the phase due to displacement (16) consists of four terms. Because of the relative order of magnitude of the variables, the phase error is most sensitive to the second term. The magnitude of the baseline (B_n) and the

DEM error (dz) are the most critical. This will be discussed in more detail in Section V.

The tensile strength of ice calculated from the strain rate has a reduced sensitivity to error. A strain rate error of 17% produces only a 5.3% error in tensile strength using either (6 or 7).

V. SENSITIVITY OF STRAIN RATE MEASUREMENT TO INSAR PARAMETERS

Further analysis of the relative error provides assessment of the strain rate sensitivity to a variety of InSAR parameters. The

$$ds = \frac{\sqrt{\left(\frac{4\pi}{\lambda \sin \theta r_0 \Delta f}\right)^2 [(z \cos(\theta - \xi) dB)^2 + (B_n dz)^2 + (z B_p d\xi)^2] + \frac{1-\rho}{N\rho^2}}}{\Delta f} \quad (16)$$

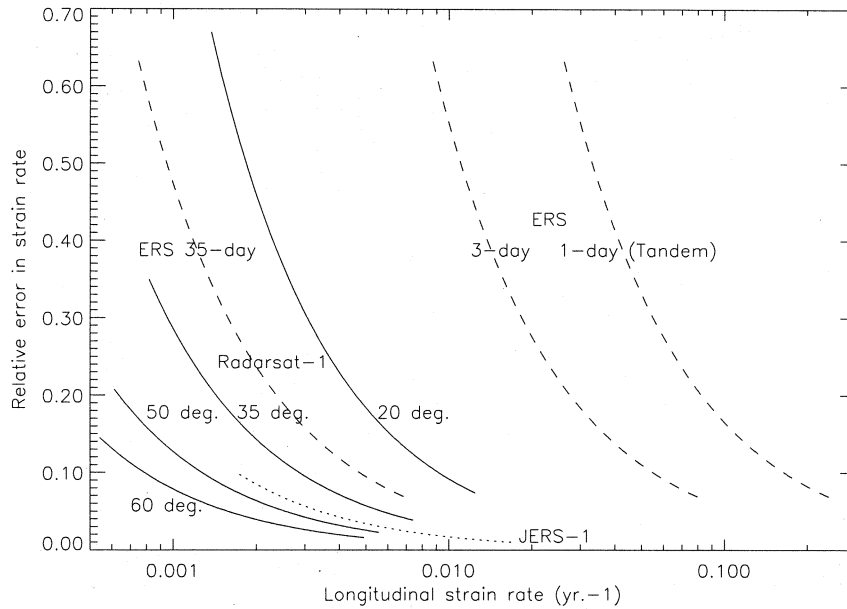


Fig. 7. Relative error in longitudinal strain rate for various InSAR datasets as a function of strain rate. The solid lines represent Radarsat-1 beam modes. The dashed lines are ERS data, and the dotted line is JERS-1.

error analysis can also provide guidelines for selecting an appropriate InSAR dataset for calculating longitudinal strain rate from the wrapped phase. The relative error (17) is a function of

$$E_R \left(\underbrace{\lambda, \theta}_{\text{SAR}}, \underbrace{B, dB, \xi, d\xi}_{\text{Baseline}}, \underbrace{\rho, N}_{\text{Proc.}}, \underbrace{dz}_{\text{DEM}}, \underbrace{z, \dot{\epsilon}_L}_{\text{Glacier}} \right)$$

which can be divided into variables of the SAR, the interferometric baseline, the InSAR processing, the DEM, and the glacier properties.

First consider the parameters defined by the SAR itself. Since changes in the wavelength and the look angle effect the relationship between the phase gradient (s) and the strain rate (8) they are evaluated as a function of strain rate. The range of strain rates used corresponds to 1–10 fringe cycles/km, beyond which the fringe rate is approaching aliased sampling at 50-m pixels. The relative error (E_R) as a function of longitudinal strain rate for the recently and presently orbiting SARs is shown in Fig. 7. Each of the error curves is defined by the wavelength, look angle and repeat time of the satellite. C-band data are available from ERS-1 and 2 at a fixed look angle of 23° and from Radarsat-1 at a variety of look angles from 10° to 60° . The standard repeat-cycle for ERS was 35 days. There was also one-day cycle data acquired when ERS-1 and 2 were flown in tandem orbits separated by a single day. Limited coverage of ERS-1 three-day repeat data are also available. Radarsat-1 is in a 24-day repeat orbit. JERS-1 operated at L-band with a look angle of 35° and repeat time of 44 days.

Longitudinal glacier strain rates can vary over three orders of magnitude from extremely high rates, for example on temperate calving glaciers, to very low rates at the interior of ice sheets. The preferred SAR parameters are dependent upon the range of strain rates anticipated. For extremely high strain rates ($>0.02 \text{ yr}^{-1}$) the short repeat times of ERS tandem or three-day data are the best option. (The longer repeat times of the other

datasets would theoretically produce less error but would likely suffer temporal decorrelation in areas with strain rates this large). Below this threshold the longer wavelength of JERS-1 is beneficial, however, the long repeat time may cause temporal decorrelation. The shorter repeat time of Radarsat-1 may be applied providing the steeper look angles are used to reduce the phase gradient produced from strain rates $>0.005 \text{ yr}^{-1}$. Below this level of strain rate the higher incidence angles available from Radarsat-1 have significantly less error.

For the remainder of the parameters in (16) and (17), the relative error (E_R) is evaluated as each is ranged over typical values with the other parameters held constant at the Recovery Glacier values. These results are shown in the last two columns of Table I. Over the typical range of baselines, and error in their estimation, used for InSAR the magnitude of the baseline (B_n) is more critical than the error in its estimation (dB_n) Table I. For example altering the B_n value over a range from 50–500 m caused the percent error to range from 4.5% to 42% respectively. In contrast, changing the baseline error (dB_n) from 1 cm to 1m causes an insignificant change in the error. The baseline tilt angle error ($d\zeta$) is varied over the range corresponding to the extremes of B_n and dB_n (resulting in 1.00° to 0.001°) but has minimal affect on the strain rate error.

The coherence of the interferogram (ρ) and the number of looks used (N) are functions of the InSAR processing. One of the factors effecting the coherence is the success of co-registering the image pairs. Non processing related effects such as changes in scattering mechanisms and large strain rates also reduce coherence. The number of looks is determined by the spatial averaging (multilooking) of the single-look complex image data to form the interferogram. Neither the coherence nor the number of looks has a significant effect on E_R .

The error in the DEM represented by dz is relative and corresponds to the pixel-to-pixel errors and not to the absolute accuracy of the DEM. This error can have a significant effect on

the ability to estimate the strain rate. Ranging dz from 1–50 m produced an error of 1.4% to 28%.

Properties of the glacier that effect E_R are the longitudinal strain rate itself, and the elevation of the glacier surface. Fig. 7 demonstrates that there is less relative error at higher strain rates for any chosen wavelength or look angle. At lower strain rates, the phase gradient is too low and the error terms in (16), which are independent of strain rate, produce a poor SNR. The error in strain rate is insensitive to glacier elevation (z) Table I.

VI. CONCLUSION

In this paper we demonstrated a technique for extracting geophysical parameters of a glacier from the wrapped phase of an InSAR interferogram. The longitudinal strain rate can be calculated from the phase gradient of the interferogram assuming the direction of ice flow is known. The tensile strength of the ice can then be calculated from the strain rate at the location of crevasse initiation making the assumptions of a simplified strain field and a predictable temperature field. SAR amplitude images typically provide the necessary information for both flow path (in the form of flow lines) and crevasse location (from increased backscatter).

An example using Radarsat-1 data of the Recovery Glacier ice stream, East Antarctica, indicated the strain rate at crevasse initiation was approximately 0.002 yr^{-1} . The corresponding tensile strength of ice ranged from 186–215 kPa depending upon the failure criteria selected. The fact that the values are within the range of tensile strength found for other East Antarctic glaciers by previous field and remote sensing investigations implies the technique may be used to increase the number of strain rate and ice strength measurements available to the glaciological community. An error analysis for the Recovery Glacier showed a strain rate error of 17% and a corresponding tensile strength error of 5.3%.

Based on reducing the relative error in strain rate calculated from wrapped phase recommendations for SAR selection and InSAR parameters are suggested. For strain rates $>0.02 \text{ yr}^{-1}$ ERS tandem or three-day repeat data are required due to the large phase gradients. For strain rates $>0.005 \text{ yr}^{-1}$ the steep look angles of Radarsat-1 Extended Low beam and Standard beam S1 or 35-day ERS data are required. Theoretically, JERS-1 could be used in this range of strain rates but, the 44-day repeat cycle would likely cause temporal decorrelation at these high strain rates. Below 0.005 yr^{-1} the shallower look angles available from Radarsat-1 Extended High beams and Standard Beam S7 have considerably less error than 35-day repeat ERS data. In general, perpendicular baselines less than 300 m with errors less than 1 m are preferred. The relative DEM error should be less than 30 m.

ACKNOWLEDGMENT

The authors would like to thank R. Bindschadler and I. Joughin for their insightful reviews that improved the manuscript.

REFERENCES

- [1] R. A. Bindschadler, P. L. Vornberger, S. N. Stephenson, E. P. Roberts, S. Shabtaie, and D. R. MacAyeal, "Ice-shelf flow at the boundary of cary ice rise, Antarctica," *Ann. Glaciol.*, vol. 11, pp. 8–13, 1988.
- [2] R. A. Bindschadler and T. A. Scambos, "Satellite-image-derived velocity field of an antarctic ice stream," *Science*, vol. 252, pp. 242–246, 1991.
- [3] R. A. Bindschadler, M. A. Fahnestock, P. Skvarca, and T. A. Scambos, "Surface-velocity field of the northern Larsen ice shelf, antarctica," *Ann. Glaciol.*, vol. 20, pp. 319–326, 1994.
- [4] H. H. Brecher, "Surface velocity determination on large polar glaciers by aerial photogrammetry," *Ann. Glaciol.*, vol. 8, pp. 22–26, 1986.
- [5] D. R. Fatland and C. S. Lingle, "InSAR observation of the 1993–1995 bering glacier (Alaska, U.S.A.) surge and surge hypothesis," *J. Glaciol.*, vol. 48, pp. 439–451, 2002.
- [6] B. Fitzharris, "The cryosphere: Changes and their impacts," in *Climate Change 1995, Impacts Adaptations and Mitigation of Climate Change: Scientific-Technical Analyses*, R. T. Watson, Ed. Cambridge, U.K.: Cambridge Univ. Press, 1996, pp. 241–265.
- [7] R. R. Forster, E. Rignot, B. L. Isacks, and K. C. Jezek, "Interferometric radar observations of glaciers europa and penguin, hielo patagnico sur, Chile," *J. Glaciol.*, vol. 45, pp. 325–337, 1999.
- [8] R. M. Goldstein, H. A. Zebker, and C. L. Werner, "Satellite radar interferometry: Two-dimensional phase unwrapping," *Radio Sci.*, vol. 23, pp. 713–720, 1988.
- [9] R. M. Goldstein, H. Engelhardt, B. Kamb, and R. M. Frolich, "Satellite radar interferometry for monitoring ice sheet motion: Application to an antarctic ice stream," *Science*, vol. 262, pp. 1525–1530, 1993.
- [10] A. L. Gray, K. E. Mattar, P. W. Vachon, R. Bindschadler, K. C. Jezek, R. R. Forster, and J. P. Crawford, "InSAR results from radarsat antarctic mapping mission data: Estimation of glacier motion using a simple registration procedure," in *Proc. IGARSS*, Seattle, WA, 1998.
- [11] R. F. Hanssen, *Radar Interferometry: Data Interpretation and Error Analysis*. Dordrecht, The Netherlands: Kluwer, 2001.
- [12] G. Holdsworth, "An examination and analysis of the formation of transverse crevasses, Kaskawulsh Glacier," Ohio State Univ., Byrd Polar Res. Center, Columbus, OH, Rep. 16, 1965.
- [13] —, "Primary traverse crevasses," *J. Glaciol.*, vol. 8, pp. 107–129, 1969.
- [14] J. C. Jaeger and N. G. W. Cook, *Fundamentals of Rock Mechanics*, 3rd ed. London, U.K.: Chapman & Hall, 1979.
- [15] K. C. Jezek, "Glaciologic properties of the antarctic ice sheet from spaceborne synthetic aperture radar observations," *Ann. Glaciol.*, vol. 29, pp. 286–290, 1999.
- [16] I. R. Joughin, K. Winerbrenner, M. Fahnestock, R. Kwok, and W. Krabill, "Measurement of ice-sheet topography using satellite-radar interferometry," *J. Glaciol.*, vol. 42, pp. 10–22, 1996.
- [17] I. R. Joughin, R. Kwok, and M. Fahnestock, "Estimation of ice-sheet motion using satellite radar interferometry: Method and error analysis with application to Humbolt Glacier, Greenland," *J. Glaciol.*, vol. 42, pp. 564–575, 1996.
- [18] I. Joughin, M. Fahnestock, R. Kwok, P. Gogineni, and C. Allen, "Ice flow of Humbolt, Petermann and Ryder Gletscher, Northern Greenland," *J. Glaciol.*, vol. 45, pp. 231–241, 1999.
- [19] I. Joughin, "Ice sheet velocity mapping: A combined interferometric and speckle tracking approach," *Ann. Glaciol.*, vol. 34, pp. 195–201, 2002.
- [20] K. Kim, *Application of Time Series Satellite Data to Earth Science Problems*. Columbus, OH: The Ohio State Univ., 1999, p. 69.
- [21] R. Kwok and M. Fahnestock, "Ice sheet motion and topography from radar interferometry," *IEEE Trans. Geosci. Remote Sensing*, vol. 34, pp. 189–199, Jan. 1996.
- [22] H. Liu, K. C. Jezek, and B. Li, "Development of an antarctic digital elevation model by integrating cartographic and remotely sensed data: A geographic information system based approach," *J. Geophys. Res.*, vol. 104, pp. 23 199–23 213, 1999.
- [23] M. F. Meier, J. E. Conel, J. A. Hoerni, W. G. Melbourne, C. J. Pings, and P. T. Walker, "Preliminary study of crevasse formation, blue ice valley, Greenland," in SPIRE Rep. 28, 1957.
- [24] M. F. Meier, "The mechanics of crevasse formation," in General Assembly of Toronto 1957—Snow and Ice, Toronto, ON, Canada, 1958.
- [25] R. Michel and E. Rigont, "Flow of Glaciari Moreno, Argentina, from repeat-pass shuttle imaging radar images: Comparison of the phase correlation method with radar interferometry," *J. Glaciol.*, vol. 45, pp. 93–100, 1999.
- [26] W. S. B. Paterson, *The Physics of Glaciers*, 3rd ed. New York: Elsevier, 1994.

- [27] J. G. Ramsay, *The Folding and Fracturing of Rocks*. New York: McGraw-Hill, 1967.
- [28] E. Rignot, R. R. Forster, and B. Isacks, "Interferometric radar observations of glacier san rafael, chile," *J. Glaciol.*, vol. 42, pp. 279–291, 1996.
- [29] G. d. Q. Robin, "General glaciology," in *The Climate Record in Polar Ice Sheets*, G. d. Q. Robin, Ed. Cambridge, U.K.: Cambridge Univ. Press, 1983, pp. 94–97.
- [30] E. Rodriguez and J. M. Martin, "Theory and design of interferometric synthetic aperture radar," *Proc. Inst. Elect. Eng. F*, vol. 139, pp. 147–159, 1992.
- [31] H. Rott, "Synthetic aperture radar capabilities for glacier monitoring demonstrated with Seasat SAR data," *Zeitschrift fur Gletscherkunde und Glazialgeologie*, vol. 16, pp. 255–266, 1980.
- [32] T. A. Scambos, K. A. Echelmeyer, M. A. Fahnestock, and R. A. Bind-schadler, "Development of enhanced ice flow at the southern margin of ice stream D, antarctica," *Ann. Glaciol.*, vol. 20, pp. 313–318, 1994.
- [33] C. J. Van der Veen, *Fundamentals of Glacier Dynamics*. Rotterdam, The Netherlands: A. A. Balkema, 1999, p. 462.
- [34] D. G. Vaughan, "Relating the occurrence of crevasses to surface strain rates," *J. Glaciol.*, vol. 39, pp. 255–266, 1993.
- [35] P. L. Vornerberger and I. M. Whillans, "Crevasse deformation and example from ice stream B, Antarctica," *J. Glaciol.*, vol. 36, pp. 3–10, 1990.
- [36] Z. Zhao, *Surface Velocities of the East Antarctic Ice Streams From Radarsat-1 Interferometric Synthetic Aperture Radar Data*. Columbus, OH: Ohio State Univ. Press, 2001, p. 180.



Richard R. Forster received the B.S. degree in electrical engineering from Lafayette College, Easton, PA, in 1984, the M.S. degree in electrical engineering from the University of Kansas, Lawrence, in 1991, and the Ph.D. degree in geophysics from Cornell University, Ithaca, NY, in 1997.

He was with Hewlett Packard, Cupertino, CA, from 1984 to 1989 before working as a Graduate Research Assistant in the Radar Systems and Remote Sensing Laboratory, University of Kansas, from 1989 to 1991. From 1991 to 1996, he was

a Graduate Research Assistant in the Department of Geological Sciences, Cornell University, working with SAR data of the Patagonian Icefields. He received the Byrd Post-Doctoral Fellowship in 1996 from the Byrd Polar Research Center (BPRC), The Ohio State University, Columbus, and then became a Senior Research Associate at BPRC in 1998. Since 1999, he has been an Assistant Professor of geography at the University of Utah, Salt Lake City, where his current research interests are in microwave remote sensing of snow and ice and InSAR applications of surface displacement.

Kenneth C. Jezek (A'92) received the Ph.D. degree in geophysics from the University of Wisconsin, Madison, in 1980.

He joined The Ohio State University, Columbus, as a Post-Doctoral Fellow in 1980. He later conducted research in various aspects of wave propagation at the U.S. Army Cold Regions Research and Engineering Laboratory before returning to Ohio State to assume Directorship of the Byrd Polar Research Center, Columbus, in 1989. After nearly ten years as Director, he became Professor in the Byrd Center, where he now leads a research team studying the earth's polar regions using satellite techniques.

Lora Koenig received the B.A. degree in mathematics from Linfield College, McMinnville, OR, in 1999, and the M.S. degree in geography from the University of Utah, Salt Lake City, in 2002. She is currently pursuing the Ph.D. degree in the Department of Earth and Space Sciences, University of Washington, Seattle.

She was a summer intern for the Environmental Systems Research Institute (ESRI), Redondo Beach, CA, in 2001. Her research interests include geographic information systems and passive microwave remote sensing of snowpack properties.



Elias Deeb received the B.S. degree in geography from the University of Utah, Salt Lake City, in 1999, and studied electrical and mechanical engineering at Lehigh University, Bethlehem, PA, from 1990 to 1994. He is currently pursuing the Ph.D. degree at the University of Utah in the remote sensing of snow for the benefit of snow hydrology applications.

He worked for Astro-Med, Inc., West Warwick, RI, from 1994 to 1998 as a Project Engineer, where he managed a research collaborative at the Laboratory for Engineering Man/Machine Systems (LEMS), Brown University, Providence, RI. From 2000 to 2002, he was a Research Assistant at the University of Utah, working with InSAR data to determine surface displacement for Antarctic glaciers. Since 1998, he has been with the Evans and Sutherland Computer Corporation, Salt Lake City, as a GIS Database Engineer creating sophisticated simulation systems for commercial and military pilot training.